JGR Solid Earth

RESEARCH ARTICLE

Key Points:
- We assess the influence of postperovskite viscosity on deep mantle dynamics and core-mantle boundary topography
- Low-viscosity postperovskite modifies deep mantle thermochemical structures
- Low viscosity strongly reduces topography beneath downwellings

Supporting Information:
- Supporting Information S1
- Data Set S1
- Data Set S2
- Data Set S3
- Data Set S4
- Data Set S5
- Data Set S6

Correspondence to:
F. Deschamps,
frederic@earth.sinica.edu.tw

Core-Mantle Boundary Dynamic Topography: Influence of Postperovskite Viscosity

Frédéric Deschamps[1] and **Yang Li[2]**

[1]Institute of Earth Sciences, Academia Sinica, Taipei, Taiwan, [2]State Key Laboratory of Lithospheric Evolution, Institute of Geology and Geophysics, Chinese Academy of Sciences, Beijing, China

Abstract Core-mantle boundary (CMB) topography may provide useful hints on the deep mantle thermochemical structure, as clusters of thermal plumes and piles of chemically differentiated material, which are usually proposed as end-member explanations for the large low shear-wave velocity regions observed in the deep mantle, have different actions on this topography. CMB topography is further sensitive to several parameters, including mantle viscosity and its variations with thermal and compositional changes. Here we assess the influence of the postperovskite (pPv) phase viscosity on deep mantle dynamics and on CMB topography. We perform numerical simulations of thermal and thermochemical convection in spherical geometry, varying the ratio between pPv and bridgmanite viscosities, $\Delta\eta_{pPv}$, between 1 (regular pPv) and 10^{-3} (weak pPv). Thermochemical structures are dominated by smaller-scale wavelengths (spherical harmonic degrees 3 to 6) and are more stable in weak than in regular pPv models. The amplitude of CMB topography is reduced by about a factor of 2 as $\Delta\eta_{pPv}$ changes from 1 to 10^{-3}, mostly due to a sharp drop in the depressions induced by downwellings reaching the CMB. By contrast, the topographies induced by plumes clusters and thermochemical piles are mostly unaffected. For all the values of $\Delta\eta_{pPv}$ we tested, long-wavelength CMB topography and reconstructed shear-wave tomography are anticorrelated in purely thermal models, and correlated in thermochemical models with strong chemical density contrast ($\Delta\rho_C = 140$ kg/m^3). In models with smaller density contrast ($\Delta\rho_C = 90$ kg/m^3), topography and tomography are anticorrelated at $\Delta\eta_{pPv} = 1$, but correlated at $\Delta\eta_{pPv} = 10^{-3}$.

1. Introduction

Seismic observations provide key observations to map deep mantle structures at different length scales, but fail to determine the nature, purely thermal or thermochemical, of these structures. For instance, the anticorrelation between anomalies in shear-wave and bulk-sound seismic velocities observed in the lowermost mantle is best explained by compositional differences between the large low-shear wave velocity provinces (LLSVPs) and the rest of the mantle (e.g., Trampert et al., 2004), but could also result from lateral variations in the stability field of the postperovskite phase (Davies et al., 2012). Observations independent from seismic travel times are therefore needed to reach a clear conclusion. Normal mode seismology brings constraints on density. Available studies mostly support denser, chemically distinct LLSVPs (Ishii & Tromp, 1999; Mosca et al., 2012; Moulik & Ekström, 2016; Trampert et al., 2004), with the exception of Stoneley mode data, which are better explained by purely thermal LLSVPs (Koelemeijer et al., 2017). Importantly, existing models of density based on normal modes rely on mode-coupling approximations that may introduce substantial bias in these models (Akbarashrafi et al., 2018; Al-Attar et al., 2012; Yang & Tromp, 2015). Additional lines of evidence support the hypothesis that LLSVPs are thermochemical structures. These include the analysis of Earth's solid tides (Lau et al., 2017), the six-year variations in the length of the day (Ding & Chao, 2018), and the joint inversion of seismic waveforms for shear-wave velocity and quality factor (Deschamps et al., 2019).

Core-mantle boundary (CMB) topography is challenging to measure accurately, in particular because it trades off with structures in the mantle and, possibly, in the outer core sides. Global models of CMB topography are based on differential travel times between topside reflected phases (*PcP*) and transmitted phases (*PKP* and *PKIKP*; Koper et al., 2003; Morelli & Dziewonski, 1987) or underside reflected phases (*PnKP*; Doornbos & Hilton, 1989; Sze & van der Hilst, 2003; Tanaka, 2010). These models are limited to spherical harmonic degrees up to $l = 4$, and strongly disagree both in amplitude and pattern. They may further be

affected by uneven raypath coverage and bouncing point distribution. Peak-to-peak amplitude ranges from 3.5 km (Koper et al., 2003) to 12 km (Morelli & Dziewonski, 1987). Maps obtained by Doornbos and Hilton (1989) and Sze and van der Hilst (2003) are dominated by spherical harmonic degree $l = 1$, while the pattern observed by Morelli and Dziewonski (1987) is more complex. The topography inferred by Tanaka (2010), which includes only spherical harmonic degrees 2 and 4, has a 5-km amplitude and is well correlated with shear-wave velocity anomalies; that is, LLSVPs are associated with depressions in the CMB. The analysis of topside and underside reflected phases further indicated that 95% of the CMB topography should be distributed between ± 4.0 km (Garcia & Souriau, 2000). Colombi et al. (2014) performed waveform inversion of *SKS* and *PKIKP* phases to map topography at selected locations due to limited coverage. The resulting topography ranges between -4.0 and 4.0 km, and is overall anticorrelated with shear-wave velocity anomalies. Constraints on topography may further be obtained from normal mode data. For spherical harmonic degree 2, normal modes indicate that peak-to-peak amplitude should not exceed 5 km (Koelemeijer et al., 2012). Finally, Soldati et al. (2013) showed that models of CMB topography deduced from geodynamically constrained tomography fit normal mode data better than topographic maps directly obtained from seismic tomography. Note, however, that this approach requires the prescription of a scaling between seismic velocity and density anomalies; that is, it implicitly assumes that chemical anomalies are small, and that they are, at a given depth, fully correlated with seismic velocity anomalies. Furthermore, the method used to constrain tomography (e.g., Forte & Peltier, 1991) does not account for lateral variations in viscosity.

Nevertheless, provided that it can be measured with precision at least locally, CMB topography may bring important constraints on the nature of deep mantle structures. More specifically, mantle flow is expected to induce dynamic topography at CMB with amplitude and pattern that depend on the deep mantle properties, in particular its distributions in viscosity and density. Thermal plumes stretch the CMB upward, while cold downwellings deflect it downward, creating topographic highs and lows, respectively. Numerical simulations of thermochemical convection indicated that the topography triggered by piles of hot and denser than average material, modeling LLSVPs, depends on the chemical density contrast $\Delta \rho_C$ between dense and regular materials. These thermochemical piles cause flat topography if $\Delta \rho_C$ is not too large (Lassak et al., 2010), typically around 90 kg/m^3 and lower, and wide depressions for larger values of $\Delta \rho_C$ (Deschamps et al., 2018). Topographies predicted by purely thermal and thermochemical cases are clearly different, but when filtered to long wavelengths (spherical harmonic degrees $l = 0$–4), to which global models of CMB topography are limited, they both anticorrelate with long wavelength shear-wave velocity anomalies (Lassak et al., 2010), unless the chemical density contrast is larger than 90 kg/m^3, in which case they correlate with these velocity anomalies (Deschamps et al., 2018).

Postperovskite (pPv) is a high-pressure phase of bridgmanite (Murakami et al., 2004; Oganov & Ono, 2004) that may be locally stable in the lowermost mantle, specifically in cold and warm regions (Hernlund et al., 2005). The presence of pPv at the base of the mantle may influence deep mantle dynamics. For instance, Nakagawa and Tackley (2005) pointed out that pPv is distributed outside thermochemical piles, and that the formation and shape of these piles depend on the Clapeyron slope of the bridgmanite to pPv phase transition, Γ_{pPv}. Numerical simulations of thermochemical convection in two-dimensional (2-D) spherical annulus geometry further indicated that the structures that match best lower mantle seismic tomography are obtained for CMB temperature around 3,750 K and Γ_{pPv} in the range 13–16 MPa/K (Li et al., 2015). By contrast, the presence of pPv does not substantially affect the dynamic topography calculated by numerical simulations, provided that the viscosity of this phase is similar to that of bridgmanite (Deschamps et al., 2018). However, ab initio calculations (Amman et al., 2010) suggested that pPv may be less viscous than bridgmanite by 2 to 3 orders of magnitude. Based on numerical simulations of convection, Li et al. (2014b) noted that low-viscosity pPv may slightly alter the stability of thermochemical piles. Because dynamic topography decreases in amplitude with decreasing viscosity, the presence of low-viscosity pPv may further alter the CMB topography pattern. Yoshida (2008), for instance, showed that a low-viscosity layer at the bottom of the mantle strongly attenuates CMB topography. If present in the deep mantle, pPv is however unlikely to surround the entire core, and its effects on CMB topography might be more limited. The main goal of this study is to explore these effects more in details, using numerical simulations of convection in full 3-D spherical geometry.

2. Modeling

To assess the influence of low-viscosity pPv on CMB topography, we run numerical simulations of thermal and thermochemical convection in spherical geometry using StagYY (Tackley, 2008). Conservation equations of momentum, mass, and energy for a compressible, infinite Prandtl number fluid are solved in 3-D spherical shells. Thermochemical simulations further solve for the conservation of composition. More specifically, thermochemical models distinguish two sorts of materials modeling the regular mantle and dense primordial material, respectively, the primordial material being initially distributed in a basal layer. Spherical shells are modeled by Yin-Yang grids sampled radially by 128 horizontal layers with grid refinement at both the top and the bottom, where thermal boundary layers are located, and around the ringwoodite-to-bridgmanite phase transition, at a depth of 660 km. Each horizontal layer is modeled with the combination of a Yin and a Yang surface of 384×128 nodes each, leading to a total lateral resolution of 512×256 points. The ratio between the radius of the core and the total radius is set to its Earth value, that is, $f = 0.55$.

The numerical setup is similar to that used in Deschamps et al. (2018), except that viscosity is allowed to vary with the fraction of pPv through the prescription of the viscosity ratio between pPv and bridgmanite, $\Delta\eta_{pPv}$. Note that the viscosity law used in our simulations (equation A6 in the supporting information) includes a yield stress, which prevents the formation of a stagnant lid at the top of the system. Mechanical boundary conditions are free-slip at both the top and the bottom of the shell. We imposed a mixed mode of heating; that is, the system is heated both from the bottom and from within. In addition, we increased the rate of internal heating in primordial material by a factor of 10 compared to the regular mantle, accounting for the possibility that this material is enriched in radiogenic elements (e.g., Kellogg et al., 1999; Richter, 1985). The total mantle heating rate is equivalent to a surface heat flux of 10 mW/m^2 and a ratio of internal to basal heating close to 0.3. Compressibility generates additional sinks and sources of heat that are controlled by the dissipation number, Di. This number varies with depth according to the radial model of thermal expansion. We fixed its surface value to $Di_S = 1.2$, and its volume average is equal to 0.43. The Rayleigh number, controlling the vigor of convection, depends on the fluid properties (density, viscosity, thermal diffusivity, and thermal expansion), which, in our setup, are allowed to vary throughout the system. As a result, there is no unique definition for this number. Here we prescribed a reference Rayleigh number Ra_0 as an input parameter, which we defined from the surface values of the thermodynamic parameters and the reference viscosity η_0, and set to 3.0×10^8 in all simulations. Depending on the simulation, this leads to an effective Rayleigh number (i.e., calculated with the volume average viscosity) between 10^6 and 2.0×10^6. In thermochemical simulations, the primordial material is initially distributed in a basal layer, whose thickness h_{DL} is determined by the volume fraction of dense material, X_{prim}. We fixed X_{prim} to 3.5% in all simulations, leading, for $f = 0.55$, to $h_{DL} = 0.068$. Details on the numerical methods and setup can be found in Tackley (2008) and Deschamps et al. (2018), and are summarized in the supporting information.

The dynamic topography at the CMB, h_{CMB}, accounts for self-gravitational effects following the approach of Zhang and Christensen (1993) and is calculated by

$$h_{CMB} = \frac{\sigma_{zz} + \Phi_{CMB}\Delta\rho_{CMB}}{\Delta\rho_{CMB}g}, \tag{1}$$

where σ_{zz} is the normal stress exerted on the CMB by the convective flow, $\Delta\rho_{CMB}$ is the density difference between the mantle and the outer core, Φ_{CMB} is the perturbation of the gravitational potential at CMB, and g is the acceleration of gravity. The normal stress is given by

$$\sigma_{zz} = 2\eta\left(\frac{\partial v_r}{\partial r} - \frac{1}{3}\nabla\cdot\boldsymbol{v}\right), \tag{2}$$

where $\boldsymbol{v}$ is the velocity, v_r is its vertical component, and η is the viscosity. The divergence of velocity in the right-hand side of equation (2) results from compressibility. Perturbations to the gravitational potential are obtained by solving Poisson's equation for a distribution of density anomalies (with respect to the reference state) that includes thermal and chemical effects, and variations in CMB topography. Compared to isostatic topography, which accounts only for the hydrostatic pressure, the dynamic topography

calculated by equation (1) includes additional contributions related to mantle flow, in particular downward deflections by cold downwellings and upward deflections by hot plumes. Isostatic topography may thus be considered as a first-order estimate of CMB topography. In purely thermal models, density excesses and reductions are correlated with downwellings and plumes, respectively, and isostatic and flow contributions add up. As a result, isostatic topography has a similar pattern but a smaller amplitude than dynamic topography. By contrast, in thermochemical models, the weight of the reservoirs of primordial material depress the CMB downward, while the dynamics of these structures push it upward. Isostatic and flow contributions are opposing each other, resulting in a more complex relationship between isostatic and dynamic topographies. For a detailed discussion on this topic, we refer to section 5.3 of Deschamps et al. (2018).

As demonstrated in earlier studies (e.g., Deschamps & Tackley, 2009; Li et al., 2014a; McNamara & Zhong, 2004), the most important parameters controlling the flow in thermochemical models are the chemical density contrast between dense and regular material, measured with the buoyancy ratio, and the thermal viscosity ratio. Sufficiently large values of the buoyancy ratio allow the formation of piles or reservoirs of dense material, the stability of which increases with increasing buoyancy ratio. If this ratio is too large, the system is chemically layered; that is, dense material forms a stable layer surrounding the core and locally pierced with holes. In all our simulations, buoyancy ratio is defined from a reference density that vary with depth following

$$B_z = \frac{\Delta\rho_c(z)}{\alpha_S\rho(z)\Delta T_S},$$

(3)

where $\Delta\rho_c(z)$ is the density contrast between dense and regular materials, α_S is the surface thermal expansion, $\rho(z)$ is the reference density at depth z, and ΔT_S is the superadiabatic temperature jump. This definition implies that the chemical density contrast needed to keep the buoyancy ratio constant changes with depth (supporting information). Another approach is to use the surface density as reference density, which leads to similar trends and results, but with buoyancy ratio shifted to slightly higher values (e.g., Li et al., 2014a). In most simulations, we set the buoyancy ratio to $B_z = 0.23$, corresponding to a chemical density contrast $\Delta\rho_C$ around 140 kg/m^3. We further run two simulations with $B_z = 0.15$, corresponding to $\Delta\rho_C$ ~90 kg/m^3. Thermal viscosity ratio is modeled with the nondimensional parameter $E_a = \ln(\Delta\eta_T)$, where $\Delta\eta_T$ is the top-to-bottom thermal viscosity ratio. In all runs, we fixed $E_a = 20.723$, corresponding to a maximum ratio of $\Delta\eta_T = 10^9$. Note, however, that due to the adiabatic increase of temperature and to the prescription of a temperature offset, the effective top-to-bottom thermal viscosity ratio is smaller than $\Delta\eta_T$ by about 2 orders of magnitude. A key role played by the thermal viscosity ratio is to control the thermal erosion of the reservoirs of dense material. Reservoirs are hotter than the surrounding mantle, and their viscosity is locally reduced by an amount that is determined by E_a. This, in turn, reduces the mechanical coupling between the reservoirs and the surrounding mantle and limits the entrainment of primordial material by thermal plumes (e.g., Deschamps & Tackley, 2008; Li et al., 2014a; Mulyukova et al., 2015). Other rheological parameters further influence this entrainment and the stability of piles. In particular the chemical (or intrinsic) viscosity ratio between primordial and regular materials, $\Delta\eta_C$, plays an opposite role to thermal viscosity ratio; that is, increasing its value promotes the erosion of reservoirs of primordial material. However, provided that internal heating is homogeneously distributed, the overall effect of increasing $\Delta\eta_C$ is to stabilize these reservoirs (Heyn et al., 2018). Here we fixed its value to $\Delta\eta_C = 30$ in all thermochemical simulations, accounting for the fact that, if primordial material is enriched in bridgmanite (Mosca et al., 2012; Trampert et al., 2004), it should be more viscous than surrounding mantle (Yamazaki & Karato, 2001). The viscosity of pPv may further influence the stability of these structures. The numerical simulations of Li et al. (2014b) showed that if pPv is less viscous than bridgmanite by 3 orders of magnitude ($\Delta\eta_{pPv} = 10^{-3}$), downwelling spreads more easily around CMB and reservoirs of primordial material are less stable than if pPv and bridgmanite have similar viscosities. This conclusion was reached assuming $\Delta\eta_C = 1$, and as demonstrated by our simulations (section 3.1) is not valid at $\Delta\eta_C = 30$.

The buoyancy and viscosity ratios further influence CMB dynamic topography, either directly or through the control they exert on the flow. Increasing the chemical density contrast locally reduces the core-mantle density contrast, $\Delta\rho_{CMB}$, and opposes pile dynamics. As a consequence, depressions beneath piles get shallower as buoyancy ratio decreases (Deschamps et al., 2018; Lassak et al., 2010). Increasing the
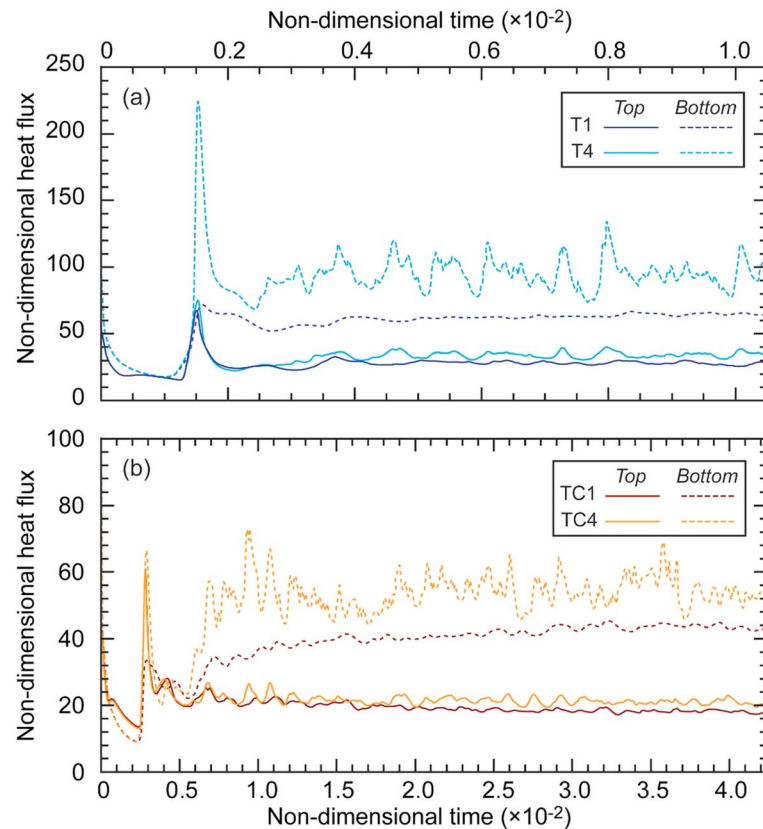
Figure 1. Time evolution of top (plain curves) and bottom (dashed curves) nondimensional heat flux for (a) purely thermal cases T1 ($\Delta\eta_{pPv} = 1$) and T4 ($\Delta\eta_{pPv} = 10^{-3}$) and (b) thermochemical cases TC1 ($\Delta\eta_{pPv} = 1$) and TC4 ($\Delta\eta_{pPv} = 10^{-3}$). Dimensional heat fluxes can be calculated by rescaling nondimensional heat fluxes with the characteristic heat flux $\Phi_c = k_S \Delta T_S / D = 2.6$ mW/m^2.

thermal viscosity ratio reduces viscosity in hot regions, plume clusters, or thermochemical piles, which results, in turn, in a reduction of the normal stress, and thus of the amplitude of dynamic topography (Deschamps et al., 2018; Lassak et al., 2010). For opposite reasons, increasing the chemical viscosity ratio deepens the depressions beneath thermochemical piles (Deschamps et al., 2018). The effects of pPv viscosity on CMB dynamic topography are explored and discussed in section 3.2.

3. Results

Using the numerical setup outlined in section 2 and supporting information, we run 10 simulations with viscosity ratio between pPv and bridgmanite ranging from 10^{-3} to 1. Cases T1, TC1, and TC5, with $\Delta\eta_{pPv} = 1$, are taken from Deschamps et al. (2018), while all other simulations were calculated for this study. Simulations are time-dependent. However, after a transient phase during which convection sets up and develops, systems statistically reach quasi steady states, as indicated by the observations that surface and bottom heat flux oscillate around constant values (Figure 1), and that amplitude in the time variations of surface heat flux are small, around 10 mW/m^2. For a given simulation, the thermochemical structures remain statistically similar; that is, plumes and piles are affected by changes in shape and location, but the type of structure remains the same. Figures 2 and 3 show representative snapshots of purely thermal cases T1 ($\Delta\eta_{pPv} = 1$) and T4 ($\Delta\eta_{pPv} = 10^{-3}$), and thermochemical cases TC1 ($B_z = 0.23$, $\Delta\eta_{pPv} = 1$) and TC4 ($B_z = 0.23$, $\Delta\eta_{pPv} = 10^{-3}$). Snapshots for cases with other values of $\Delta\eta_{pPv}$ are plotted in Figures S1 and S2 in the supporting information, and cases with $B_z = 0.15$ are discussed in section 3.3. Table 1 lists average properties, including average temperature, top and bottom heat fluxes, and root mean square (*rms*) of surface velocities for each of these snapshots.
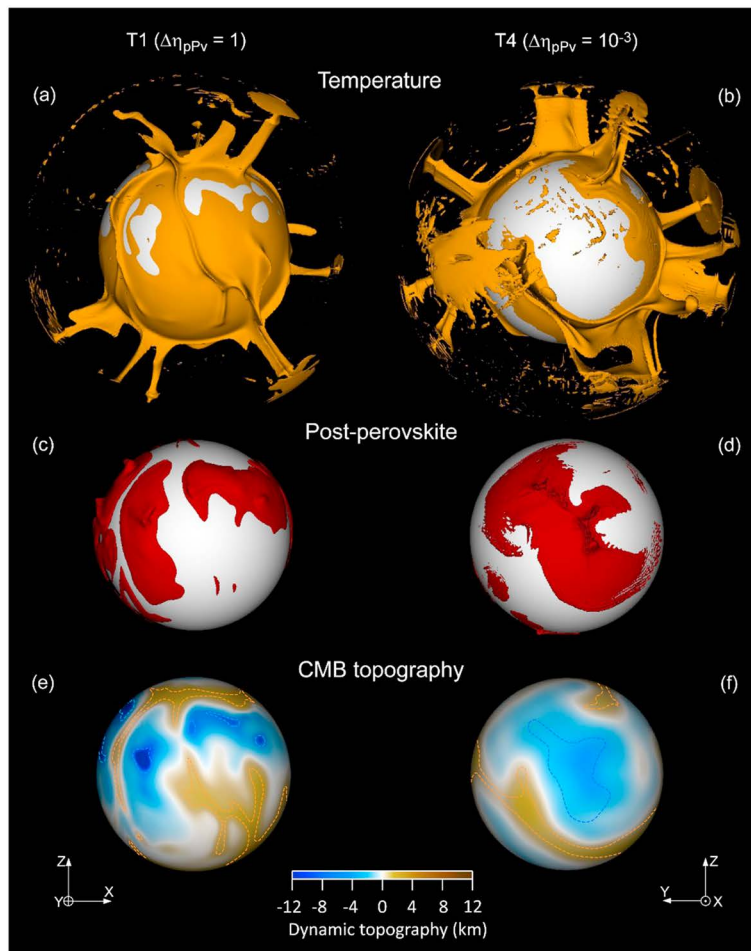
Figure 2. Snapshots of purely thermal cases with postperovskite viscosity ratio (left column) $\Delta\eta_{pPv} = 1$ (T1) and (right column) $\Delta\eta_{pPv} = 10^{-3}$ (T4) at nondimensional time $t = 0.636 \times 10^{-2}$. (a and b) Isosurface of the nondimensional temperature for $T = 0.80$. (c and d) Stability field of the postperovskite phase. (e and f) Core-mantle boundary dynamic topography (color scale). The orange and blue dotted lines in (e) and (f) indicate the limits of the plumes and downwelling regions, respectively. Run properties are listed in Table S1 in the supporting information.

The prescription of a yield stress in the viscosity law prevents the formation of a stagnant lid at the top of the system. In our simulations, the *rms* surface velocities range from 0.6 cm/year (case TC3) to 3.1 cm/year (case T2; Table 1). Note that surface velocity is overall larger in purely thermal cases (from 1.9 to 3.1 cm/year) than in thermochemical cases (from 0.6 to 1.0 cm/year). Mobility, defined as the ratio between the *rms* of surface velocity and the *rms* of velocity over the entire shell, varies between 0.95 (case TC3) and 1.57 (case TC1), and is, again, overall larger in purely thermal cases than in thermochemical models. By contrast, surface velocity and mobility do not follow clear and regular trends as a function of $\Delta\eta_{pPv}$. Mobilities close to or larger than 1 indicate that, while they do not specifically include plate tectonics, our simulations have a mobile surface that mimic this process.

3.1. Thermochemical Structure

Thermochemical cases with $B_z = 0.23$ are colder than purely thermal cases with similar $\Delta\eta_{pPv}$ by about 250–300 K (Table 1), except in the lowermost 300 km, where thermochemical cases are hotter by 50–100 K, due to the presence of dense, hot material. As noted by Li et al. (2014b), mantle temperature slightly increases with decreasing pPv viscosity (Figure S3 in the supporting information), suggesting that cooling gets less efficient as pPv is weaker. In purely thermal cases, weak pPv ($\Delta\eta_{pPv} = 10^{-3}$) models are hotter than regular pPv ($\Delta\eta_{pPv} = 1$) models by 110 K. In thermochemical cases, this difference is slightly larger, around 160 K. An
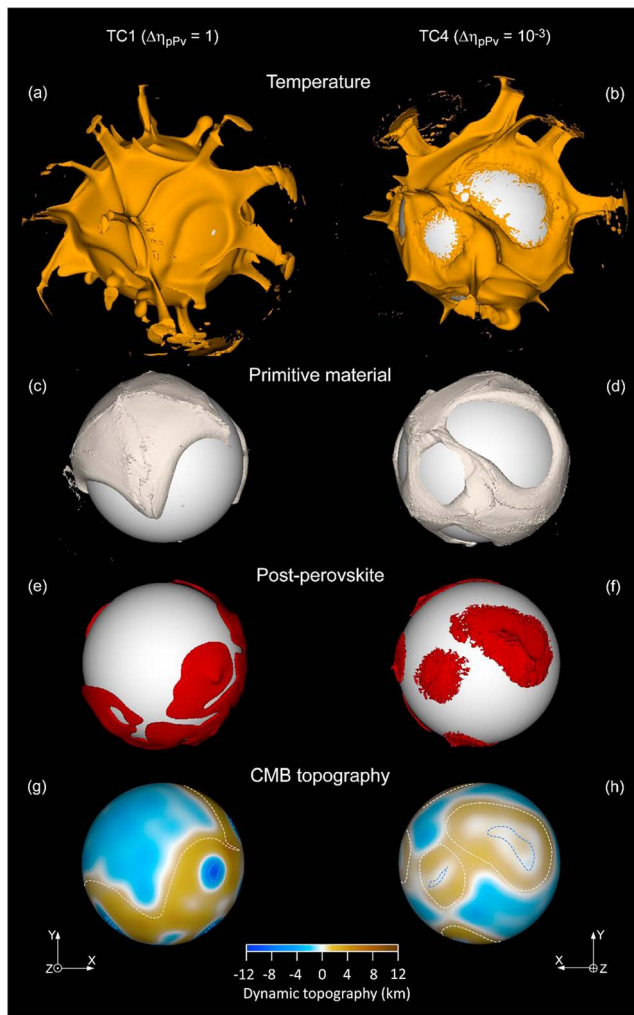
Figure 3. Snapshots of thermochemical cases with buoyancy ratio $B_z = 0.23$ and postperovskite viscosity ratio (left column) $\Delta\eta_{pPv} = 1$ (TC1) and (right column) $\Delta\eta_{pPv} = 10^{-3}$ (TC4) at nondimensional time $t = 3.5 \times 10^{-2}$. (a and b) Isosurface of the nondimensional temperature for $T = 0.67$ (TC1) and $T = 0.72$ (TC4). (c and d) Isosurface of the composition for $C = 0.5$. (e and f) Stability field of the postperovskite phase. (g and h) Core-mantle boundary dynamic topography (color scale). The white and blue dotted lines in (g) and (h) indicate the limits of the reservoirs of dense material and of downwelling regions, respectively. Run properties are listed in Table S1 in the supporting information.

interesting observation is that temperature anomalies right above the CMB strongly increase in amplitude as pPv gets weaker, with *rms* anomalies for weak pPv cases being larger by about a factor of 2 compared to regular pPv cases (Table 1). A closer examination shows that this increase is mostly due to strong negative temperature anomalies related to arrival of downwellings at the CMB.

Downwellings affect the thermochemical structure of the deep mantle. In particular, the shapes and locations of reservoirs of dense material are partially controlled by the distribution and geometry of downwellings (e.g., Bower et al., 2013). In our simulations, downwellings initiate as long sheets of cold material close to the surface, and split in smaller scale, but still horizontally elongated, structures, at greater depths (Figure S4 in the supporting information). Note that in purely thermal cases long and thin sheets are more easily maintained at greater depths. At the bottom of the shell, downwellings spread around the CMB and, in thermochemical cases, interact with primordial material.

Heat flux is higher in purely thermal cases and increases with decreasing pPv viscosity (Figure 1). Surface heat flux is around 80 mW/m^2 for model T1, and 90 mW/m^2 for model T4. For thermochemical models, surface heat flux is smaller, in the range 45–55 mW/m^2. One may point out that except for purely thermal case with weak pPv, surface heat fluxes from our simulations are rather low compared to the average surface heat flux estimated for the Earth, around 86 mW/m^2 (Davies, 2013). However, because it includes a crustal heat contribution of about 8 TW (Jaupart et al., 2015), the observed surface heat flux is likely overestimating the heat flux at the top of the mantle. In addition, mantle secular cooling may contribute up to half of Earth's surface heat loss (Jaupart et al., 2015), but is not included in our models. Bottom heat flux is around 160 mW/m^2 for case T1 and 260 mW/m^2 for case T4, equivalent to powers of 24 and 40 TW, respectively. For cases TC1 and TC4 it drops to 110 and 160 mW/m^2, corresponding to powers of 17 and 24 TW. By comparison, the core heat flow is expected to be in the range 5–17 TW. It is further interesting to note, as previously observed by Li et al. (2014b), that time variations of heat flux are much more pronounced in weak pPv cases. For instance, variations in CMB heat flux have amplitudes of 50 mW/m^2 for TC4 and 100 mW/m^2 for T4. By comparison, amplitude in heat flux variations reaches only 10 mW/m^2 for regular pPv cases.

The thermal and chemical structures are substantially affected by changes in the viscosity of pPv. Spectral heterogeneity maps of temperature distribution (Figures 4 and S5 in the supporting information), plotting power spectra of the temperature field as a function of depth, shows that the dominant wavelength of temperature anomalies slightly decreases with $\Delta\eta_{pPv}$, from spherical harmonic degrees $l = 2$–3 for $\Delta\eta_{pPv} = 1$ to $l = 4$–8 for $\Delta\eta_{pPv} = 10^{-3}$. In addition, short-scale ($l > 12$) temperature anomalies are smoothed out as pPv viscosity decreases. In thermochemical simulations, the size and shape of thermochemical reservoirs strongly vary with $\Delta\eta_{pPv}$ (Figures 3 and S2 in the supporting information). For $\Delta\eta_{pPv} = 1$, hot primordial material is distributed in two large antipodal reservoirs, while for $\Delta\eta_{pPv} = 10^{-3}$, it forms a continuous layer pierced with large holes, quite similar to the structures obtained for larger buoyancy ratio (Deschamps et al., 2018). Reservoirs of primordial material thus appear to be more stable as pPv viscosity decreases. This hypothesis is supported by two observations. First, the average nondimensional altitude of dense material (supporting information), which is a measure of the efficiency of mixing between primordial and regular materials (Deschamps & Tackley, 2008), decreases with decreasing $\Delta\eta_{pPv}$, from 0.129 for TC1 to 0.084 for TC4 (Table 1). Second, the fraction of CMB area covered by dense material, ζ_{CMB}, increases with decreasing

Table 1
Some Average Properties of Purely Thermal (T) and Thermochemical (TC) Simulations

Run	B	$\Delta\eta_{pPv}$	$<T>$ (K)	*rms* in dT_{bot} (K) Global	Negative	Positive	Φ_{top} (mW/m^2)	Φ_{bot} (mW/m^2)	V_{surf} (cm/year)	M	$<h_C>$	ζ_{CMB}
T1	-	1	2490	190	240	150	80.4	162.7	2.3	1.49	-	-
T2	-	10^{-1}	2530	330	460	230	92.2	206.2	3.1	1.51	-	-
T3	-	10^{-2}	2570	350	490	235	80.4	213.7	1.9	1.24	-	-
T4	-	10^{-3}	2600	370	540	235	93.9	269.6	2.7	1.24	-	-
TC1	0.23	1	2160	230	270	180	48.5	114.6	1.0	1.57	0.129	0.430
TC2	0.23	10^{-1}	2240	350	490	230	53.5	131.7	1.0	1.38	0.103	0.532
TC3	0.23	10^{-2}	2300	365	540	230	53.7	131.6	0.6	0.95	0.096	0.572
TC4	0.23	10^{-3}	2320	415	660	240	54.7	157.4	0.8	0.96	0.084	0.667
TC5	0.15	1	2260	180	190	175	47.3	119.2	0.6	1.09	0.279	0.300
TC6	0.15	10^{-3}	2420	390	550	260	62.0	172.1	1.0	1.00	0.109	0.526

Listed properties are the volume average temperature, $<T>$; root mean square in global, negative, and positive temperature anomalies in the lowermost 50 km layer, *rms* (dT_{bot}); top and bottom dimensional heat fluxes, Φ_{top} and Φ_{bot}; *rms* of surface velocity, V_{surf}, mobility, M, average non-dimensional altitude of dense material, $<h_C>$ (equation A3); and fraction of the CMB surface covered by dense material, ζ_{CMB}.

pPv viscosity. A possible explanation for this behavior is that because downwelling regions in weak pPv simulations are less viscous, their ability to push away and destabilize reservoirs of primordial material is reduced. This conclusion, however, is in contradiction with that drawn by Li et al. (2014b). This discrepancy is likely related to differences in the assumed chemical viscosity contrast, which is fixed to 30
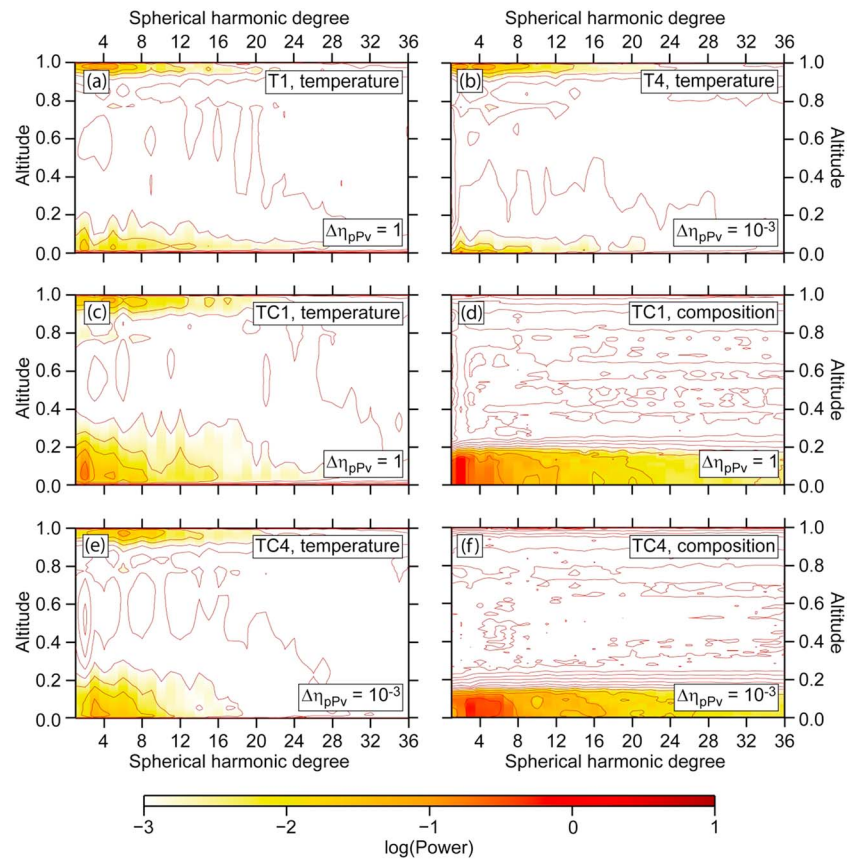
Figure 4. Spectral heterogeneity maps of temperature and compositional (if applicable) fields for purely thermal simulations T1 and T4, and thermochemical simulations TC1 and TC4. (a) Case T1. (b) Case T4. (c and d) Case TC1. (e and f) Case TC4. Power is plotted in logarithmic scale, and contour lines are plotted every log(P) = 0.5. Similar maps for other cases are shown in Figure S5 in the supporting information.

Table 2
Core-Mantle Boundary (CMB) Topography for Purely Thermal (T) and Thermochemical (TC) Simulations With Different Viscosity of Postperovskite, $\Delta\eta_{pPv}$

Run	B_z	$\Delta\eta_{pPv}$	rms (km)	$<h_{hot}>$ (km)	$<h_{cold}>$ (km)	Peak-to-peak amplitude (km) $l = 2$	$l = 0–4$	Full	$x_{4\ km}$	χ $l = 0–4$
Run										
T1	-	1	2.4	2.4	−8.9	4.5	7.7	19.0	0.913	−0.83
T2	-	10^{-1}	2.3	2.2	−8.2	4.1	8.3	15.7	0.940	−0.81
T3	-	10^{-2}	1.5	1.5	−4.0	3.2	6.6	8.4	0.995	−0.87
T4	-	10^{-3}	1.4	1.3	−3.8	2.9	5.4	8.0	0.996	−0.93
TC1	0.23	1	2.8	−1.1	−7.5	4.6	7.1	19.5	0.873	0.54
TC2	0.23	10^{-1}	2.0	−0.9	−4.8	2.8	6.2	13.3	0.982	0.64
TC3	0.23	10^{-2}	1.9	−1.2	−0.5	1.9	6.4	10.0	0.993	0.85
TC4	0.23	10^{-3}	1.7	−0.8	0.2	2.3	5.6	8.2	0.999	0.86
TC5	0.15	1	2.2	0.4	−7.4	2.7	5.6	17.8	0.939	−0.50
TC6	0.15	10^{-3}	1.2	−0.6	−0.3	0.9	4.0	7.1	0.999	0.72
Observations										
KDT12						≤5.0				
MD87							12.0			
DH89							8.0			
SV03							4.0			
KPF03							3.5			
T10							5.0			
GS00									0.950	

Except for the values of $\Delta\eta_{pPv}$ and of the buoyancy ratio B_z, all runs have the same physical and rheological properties (see supporting information and Table S1). CMB topography statistics includes *rms* of global topography, and average topography in primordial reservoirs or plume clusters, $<h_{hot}>$, and in slab areas $<h_{cold}>$. Also listed are the peak-to-peak topography filtered for spherical harmonic degrees $l = 2$, and $l = 0–4$, the full peak-to-peak topographic amplitude, the fraction of CMB with topography between −4.0 and 4.0 km, $x_{4\ km}$, and the correlation χ between long-wavelength ($l = 0–4$) dynamic topography and shear velocity anomalies predicted by each model of convection (see also Figure 5). Seismological observation are from Koelemeijer et al. (2012) (KDT12), Morelli and Dziewonski (1987), Doornbos and Hilton (1989) (DH89), Sze and van der Hilst (2003) (SV03), Koper et al. (2003), Tanaka (2010), and Garcia and Souriau (2000) (GS00). Note that topography from Tanaka (2010) is for spherical harmonic degrees 2 and 4 only. All topographies are given in km.

in this study and 1 in Li et al. (2014b), suggesting that the influence of viscosity changes on the stability of reservoir of primordial material is more complex and should integrate thermal, compositional, and phase contributions to viscosity changes (section 5). It is further interesting to note that like temperature distributions, lateral variations in composition are progressively dominated by shorter wavelengths as $\Delta\eta_{pPv}$ decreases, from spherical harmonic degree $l = 2$ for $\Delta\eta_{pPv} = 1$ to $l = 3–6$ for $\Delta\eta_{pPv} = 10^{-3}$ (Figures 4 and S5). An interesting consequence is that seismic velocity anomalies associated with these thermal and compositional changes are also dominated by shorter wavelengths as $\Delta\eta_{pPv}$ decreases (section 4).

3.2. CMB Topography

Table 2 and Figure 5 compare *rms* and amplitude of topography predicted by our simulations. For both purely thermal and thermochemical models, *rms* topography decreases with decreasing $\Delta\eta_{pPv}$ by about 1 km. The decrease in peak-to-peak amplitude is even more spectacular. In both thermal and thermochemical cases, amplitude drops from about 20 to 8 km as $\Delta\eta_{pPv}$ decreases from 1 to 10^{-3}. A closer examination indicates that most of this decrease is related to a sharp drop in the depth of the depressions induced by the arrival of downwellings at the CMB (downwellings, plumes, and piles regions are defined in the supporting information). In purely thermal cases, the average depth (Table 2) and *rms* topography (Figure 5a) in these regions decrease from ~9 km for $\Delta\eta_{pPv} = 1$ (model T1) to less than 4 km for $\Delta\eta_{pPv} = 10^{-3}$ (model T4). In thermochemical cases, the average topography in the downwelling regions changes from −7.5 km for $\Delta\eta_{pPv} = 1$ (model TC1) to a slightly positive value, at 0.2 km, for $\Delta\eta_{pPv} = 10^{-3}$ (model TC4), while *rms* topography drops from 7.7 to 0.7 km. In this later case, the absolute topographic minimum remains negative, around −1.0 km. By contrast, in hot regions, corresponding to plume areas in purely thermal simulations and thermochemical piles in thermochemical models, average topography is only slightly affected by the viscosity of pPv. As $\Delta\eta_{pPv}$ changes from 1 to 10^{-3}, it is reduced by about 1 km beneath plumes, and remains nearly unchanged beneath thermochemical piles, with *rms* around 2
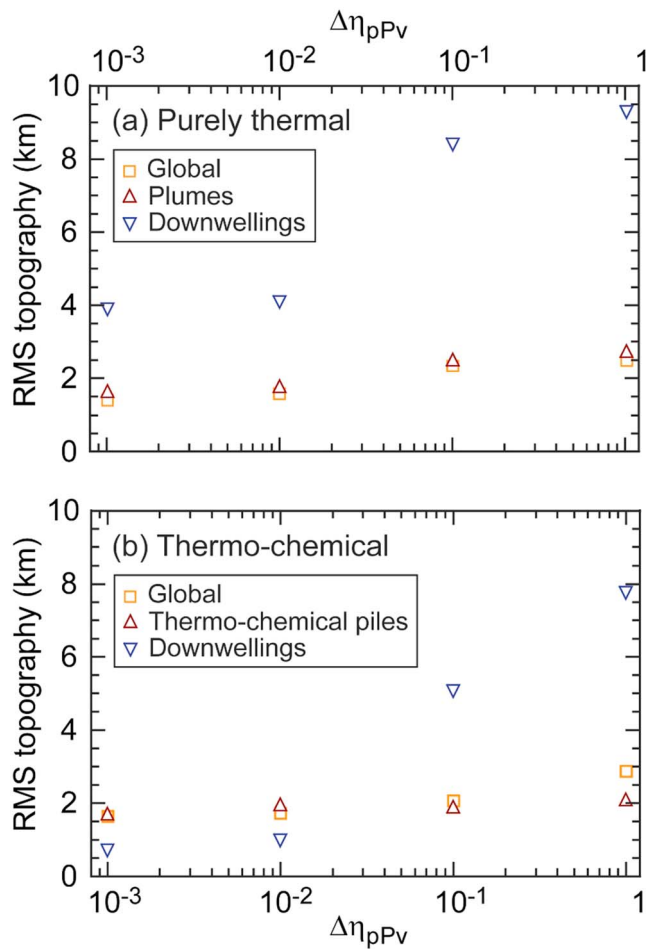
Figure 5. Root mean square (RMS) in core-mantle boundary (CMB) dynamic topography as a function of the viscosity ratio between postperovskite and bridgmanite, $\Delta\eta_{pPv}$, for (a) purely thermal and (b) thermochemical simulations. RMS are calculated over the whole CMB area (orange symbols), in plumes or thermochemical piles regions (dark red symbols), and in downwelling regions (blue symbols).

km. As a result, in thermochemical models with low pPv viscosity, downwellings are no longer associated with deep depressions corresponding to absolute topographic minima, but with local topographic minima, while absolute minima are located within the depressions caused by thermochemical piles (Figures 3h and S2h).

The changes in CMB topography with pPv viscosity can easily be understood if one remembers that pPv is present only in the coldest parts of the models, and is thus mainly associated with downwellings (Figures 2 and 3). If pPv viscosity is low, the depressions caused by downwellings are limited in amplitude. A related effect is that the topographic distributions become less dispersed as $\Delta\eta_{pPv}$ decreases (Figures 6 and S6 in the supporting information). In particular, the skewness toward large negative topography, which is associated with downwellings and is clearly present at $\Delta\eta_{pPv} = 1$, disappears as $\Delta\eta_{pPv}$ decreases. Note that, while it decreases with decreasing $\Delta\eta_{pPv}$, the range of topography predicted by numerical simulations remains in good agreement with the observation that 95% of the CMB topography ranges from -4.0 to 4.0 km (Garcia & Souriau, 2000) for all explored values of $\Delta\eta_{pPv}$. For cases with $\Delta\eta_{pPv} = 1$, about 90% of CMB topography is distributed between -4.0 and 4.0 km, while for $\Delta\eta_{pPv} = 10^{-3}$ the entire topography fits within this range.

For comparison with the CMB topography observed by global seismic models, the topography predicted by numerical simulations must be filtered for very long wavelength (spherical harmonic degrees up $l = 4$). The amplitude of long-wavelength topography follows the same trend as that of full topography; for example, it decreases with decreasing $\Delta\eta_{pPv}$ (Table 2). A difference, however, is that the drop in peak-to-peak amplitude is much reduced. For both $l = 2$ and $l = 0$–4 spherical harmonic filters, it decreases by about 2 km as $\Delta\eta_{pPv}$ changes from 1 to 10^{-3}. Again, this is easily explained by the fact that the strongest changes in CMB topography with $\Delta\eta_{pPv}$ occur in downwelling regions. Because downwellings are local structures, the topography they induce is smoothed out at long wavelengths. For $l = 2$, all models predict a peak-to-peak amplitude lower than 5.0, thus satisfying observational constraint from normal mode data (Koelemeijer et al., 2012; Table 2). For $l = 0$–4, models T1 and TC1, with $\Delta\eta_{pPv} = 1$, have a peak-to-peak amplitude slightly lower than 8 km, in

agreement with amplitude of the global CMB topography maps obtained by Doornbos and Hilton (1989) (Table 2), while for models T4 and TC4, with $\Delta\eta_{pPv} = 10^{-3}$, amplitude is around 5.0 km, slightly higher than that observed by Sze and van der Hilst (2003), at 4.0 km.

Overall, decreasing the viscosity of pPv by 2 to 3 orders of magnitude reduces the amplitude of CMB topography by about a factor of 2 for both purely thermal and thermochemical simulations. This reduction is essentially related to a strong decrease in the depth of the depressions caused by cold downwellings, where pPv is mostly present. Because these regions extend over limited areas, the decrease in *rms* amplitude is more modest, about 1 km, and the decrease in amplitude at long wavelengths is less pronounced. Interestingly, long-wavelength peak-to-peak amplitudes remain consistent with those predicted by seismic observations.

3.3. Weak Thermochemical Cases

The main parameter controlling the stability of reservoirs of dense material is buoyancy ratio (Deschamps & Tackley, 2009; Li et al., 2014a; McNamara & Zhong, 2004). To test the effect of low viscosity of pPv on thermochemical models with small chemical density contrasts, we run two additional cases (TC5 and TC6) with $B_z = 0.15$, corresponding to chemical density contrast around 90 kg/m^3. For a given value of $\Delta\eta_{pPv}$, the temperature and heat flux of weak thermochemical cases are intermediate between those of purely thermal and strong (i.e., $B_z = 0.23$) thermochemical cases (Table 1). More precisely, weak thermochemical cases are

Figure 6. Distribution histograms of core-mantle boundary dynamic topography for (a and b) purely thermal cases T1 and T4 and (c and d) thermochemical cases TC1 and TC4. The brackets in legends indicate the topographic range (in km) for each case. The viscosity ratio between postperovskite and bridgmanite is $\Delta\eta_{pPv} = 1$ for cases T1 and TC1, and $\Delta\eta_{pPv} = 10^{-3}$ for cases T4 and TC4. In thermochemical cases, the buoyancy ratio is set to $B_z = 0.23$. All other properties are listed in Table S1 in the supporting information. Frequency is normalized to the total area of the CMB. For convenience, histograms are truncated to the interval $[-10, 10]$ km, implying that topography caused by down-wellings in cases T1 and TC1 is not entirely represented. Similar histograms for other cases are shown in Figure S6 in the supporting information.

colder than purely thermal models by 150–200 K (Figure S3 in the supporting information), while their top and bottom heat fluxes are up to 65 and 180 mW/m^2 for the weak pPv model (TC6), that is, slightly larger than those obtained for strong thermochemical cases. Figure 7 plots snapshots of cases TC5 ($\Delta\eta_{pPv} = 1$) and TC6 ($\Delta\eta_{pPv} = 10^{-3}$). Due to stronger entrainment of dense material, changes in the shape and size of thermochemical piles are more important than in strong thermochemical cases. Interestingly, the fraction of CMB area covered with dense material is larger in the weak pPv case (TC6) than is the regular pPv model (TC5), while average altitude of dense material follows the opposite trend. These observations, together with Figure 7, suggest that dense reservoirs are overall more stable in the weak pPv cases. Finally, changes in CMB topography with $\Delta\eta_{pPv}$ follow the trend observed for purely thermal and strong thermochemical cases; that is, topographic amplitude is reduced as $\Delta\eta_{pPv}$ decreases (Table 2), mostly due to a strong decrease in the depths of the depressions induced by slabs.

4. CMB Topography and Shear-Wave Velocity Tomography

Plume clusters stretch the CMB upward and induce positive topography with amplitude that depends on the local viscosity (Deschamps et al., 2018; Lassak et al., 2010). By contrast, hot thermochemical piles induce depressions in the CMB, of amplitude that depends on both the chemical density contrast and the local viscosity. As a result, one expects that CMB topography and shear-wave velocity anomalies (dlnV_S) close to the CMB are anticorrelated in purely thermal models, where negative dlnV_S (due to higher than average temperatures) are associated with plume clusters, and correlated in thermochemical models, where negative dlnV_S (due to a combination of thermal and compositional effects) are associated with thermochemical piles. Existing global models of CMB tomography are however limited to very long wavelengths, up to spherical harmonics degree $l = 4$. When CMB topography predicted from numerical simulations is filtered to these wavelengths, the shallow depressions induced by piles with small to moderate chemical density contrast (typically, $\Delta\rho_C \leq 90$ kg/m^3) are smoothed out, and the resulting topography is anticorrelated with long-wavelength dlnV_S (Lassak et al., 2010). Piles with larger density contrasts induce deeper depressions, which allow to maintain a correlation between topography and shear-wave tomography (Deschamps et al., 2018).
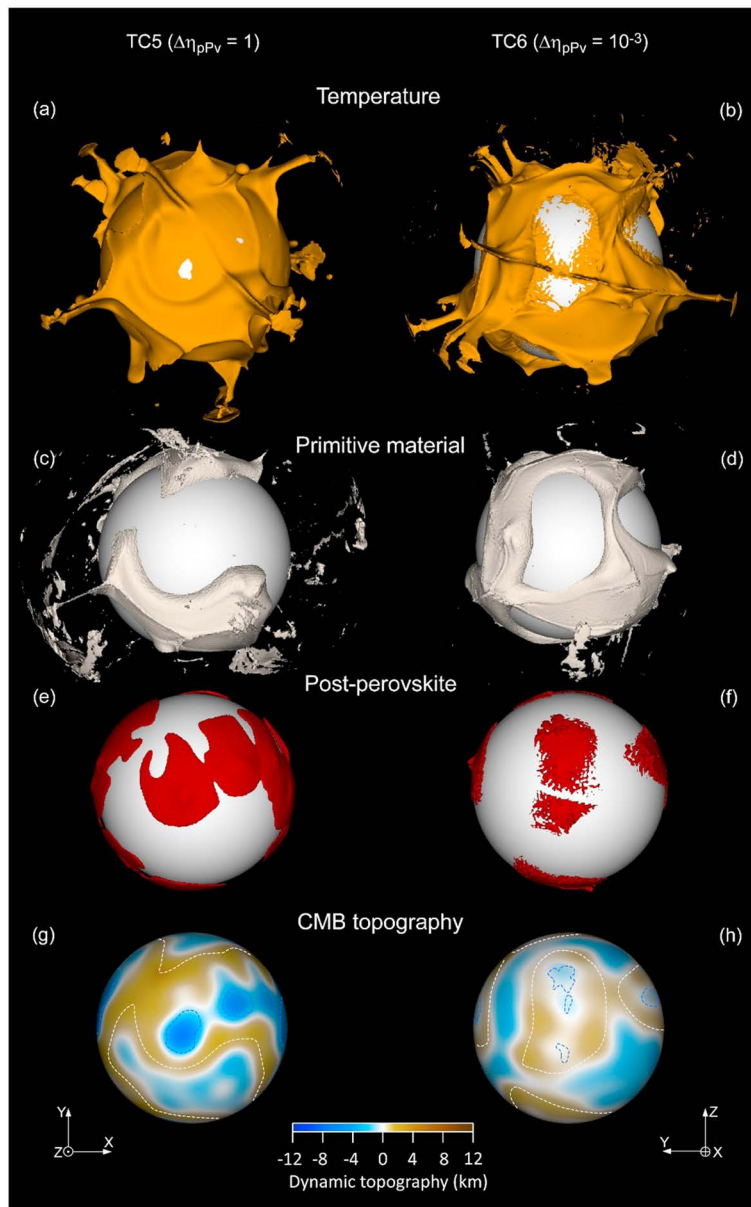
Figure 7. Snapshots of thermochemical cases with buoyancy ratio $B_z = 0.15$ and postperovskite viscosity ratio (left column) $\Delta\eta_{pPv} = 1$ (TC5) and (right column) $\Delta\eta_{pPv} = 10^{-3}$ (TC6) at nondimensional time $t = 3.18 \times 10^{-2}$ and $t = 1.27 \times 10^{-2}$, respectively. (a and b) Isosurface of the nondimensional temperature for $T = 0.72$ (TC5) and $T = 0.76$ (TC6). (c and d) Isosurface of the composition for $C = 0.5$. (e and f) Stability field of the postperovskite phase. (g and h) Core-mantle boundary dynamic topography (color scale). The white and blue dotted lines in (g) and (h) indicate the limits of the reservoirs of dense material and of downwelling regions, respectively. Run properties are listed in Table S1 in the supporting information.

To explore the role of pPv viscosity on the correlation between topographic and tomographic maps, we calculated seismic velocity anomalies predicted by the thermal and chemical variations obtained from our numerical simulations. Because in these simulations all calculations are performed in nondimensional units, the temperature fields have to be rescaled with the superadiabatic temperature jump, here assumed to be 2,500 K, prior to the calculation of seismic velocities. The adiabatic increase of temperature with pressure is taken into account when solving the energy and momentum conservation equations, but for practical reasons, the output temperatures are uncompressed, and must be corrected again for the pressure effects. This is done by multiplying the output temperatures at a given depth by an adiabatic correction defined
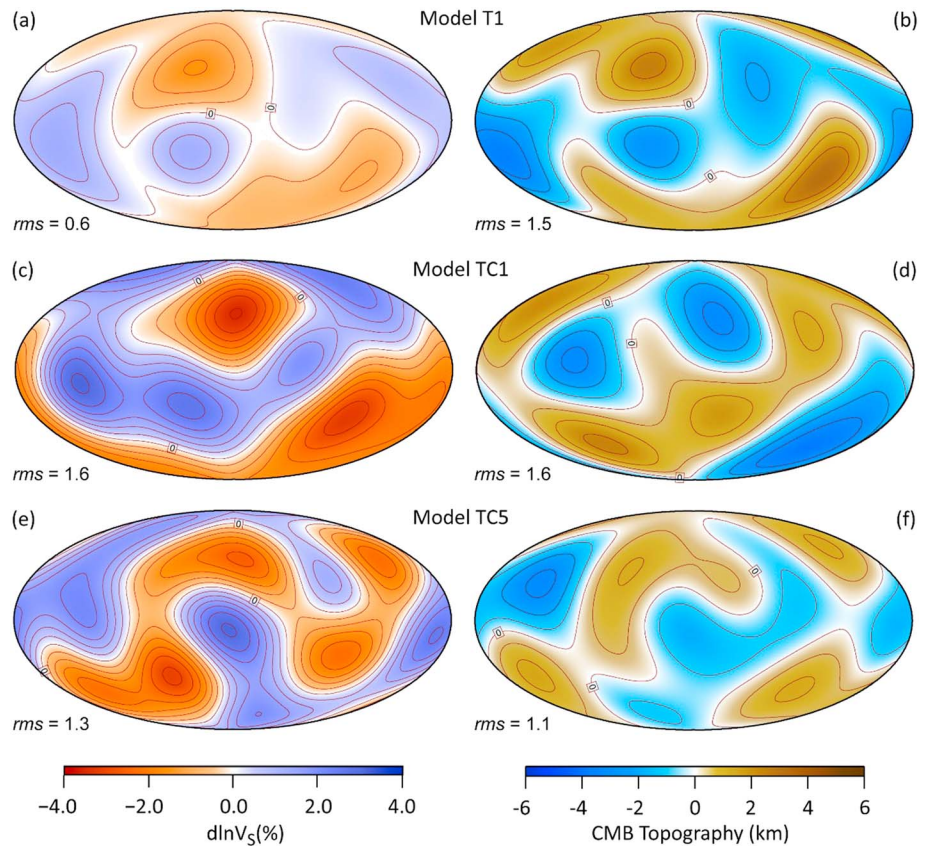
Figure 8. Shear-wave velocity anomalies in the (left column) lowermost mantle (2,700–2,891 km) and (right column) CMB dynamic topography predicted by (top row) purely thermal model T1 and thermochemical models (middle row) TC1 ($B_z = 0.23$) and (bottom row) TC5 ($B_z = 0.15$). The viscosity ratio between postperovskite and bridgmanite is $\Delta\eta_{pPv} = 1$ in all plots. All maps are filtered for spherical harmonic degrees up to $l = 4$. For details on the calculation of shear-wave velocity anomalies, see main text and supporting information. Intervals of contour levels are 0.5% for $dlnV_S$ and 1 km for CMB topography. Root mean square (*rms*) of each distribution is indicated at the bottom left of each plot.

from the radial model of thermal expansion (supporting information). After adiabatic correction and rescaling, the *rms* in temperature anomalies in the lowermost 400 km are around 300 K in purely thermal simulations, and 500 K in thermochemical cases. The compositional field is also nondimensional, varying from $C = 0$ for regular material, and $C = 1$ for primordial material. The nature of regular and primordial material is not a priori prescribed in the simulations, and should thus be specified. Here we assumed that the regular composition is pyrolitic, and that the primordial material is enriched in iron oxide by 3% and in bridgmanite by 18%. Shear-wave velocity anomalies are calculated from the rescaled temperature anomalies and compositional fields using the method and seismic sensitivities of Deschamps et al. (2012) (Figure S7 in the supporting information), except for the sensitivity to postperovskite, which we fixed to 2.0×10^{-2}, based on the compilation of Cobden et al. (2015). These anomalies are then radially averaged according to the parameterization of the tomographic model SB10L18 (Masters et al., 2000), in which the lowermost layer samples the depth range 2,700–2,891 km, and filtered for spherical harmonic degrees up to $l = 4$. Resulting maps of $dlnV_S$ for $\Delta\eta_{pPv} = 1$ and $\Delta\eta_{pPv} = 10^{-3}$ are plotted in Figures 8 and 9 (for other values of $\Delta\eta_{pPv}$, see Figure S8 in the supporting information) together with maps of filtered dynamic topographies, and correlations between these two distributions are listed in Table 2. As expected, in purely thermal simulations, long-wavelength CMB topography variations anticorrelate with predicted $dlnV_S$. This anticorrelation is more pronounced for weak pPv cases, reaching $\chi = -0.93$ for model T4 ($\Delta\eta_{pPv} = 10^{-3}$). In strong thermochemical cases ($B_z = 0.23$), long-wavelength CMB topography correlates with predicted $dlnV_S$, and this correlation becomes, again, stronger with decreasing pPv viscosity, up to $\chi = 0.86$ for case TC4 ($\Delta\eta_{pPv} = 10^{-3}$). By contrast, for weak thermochemical cases
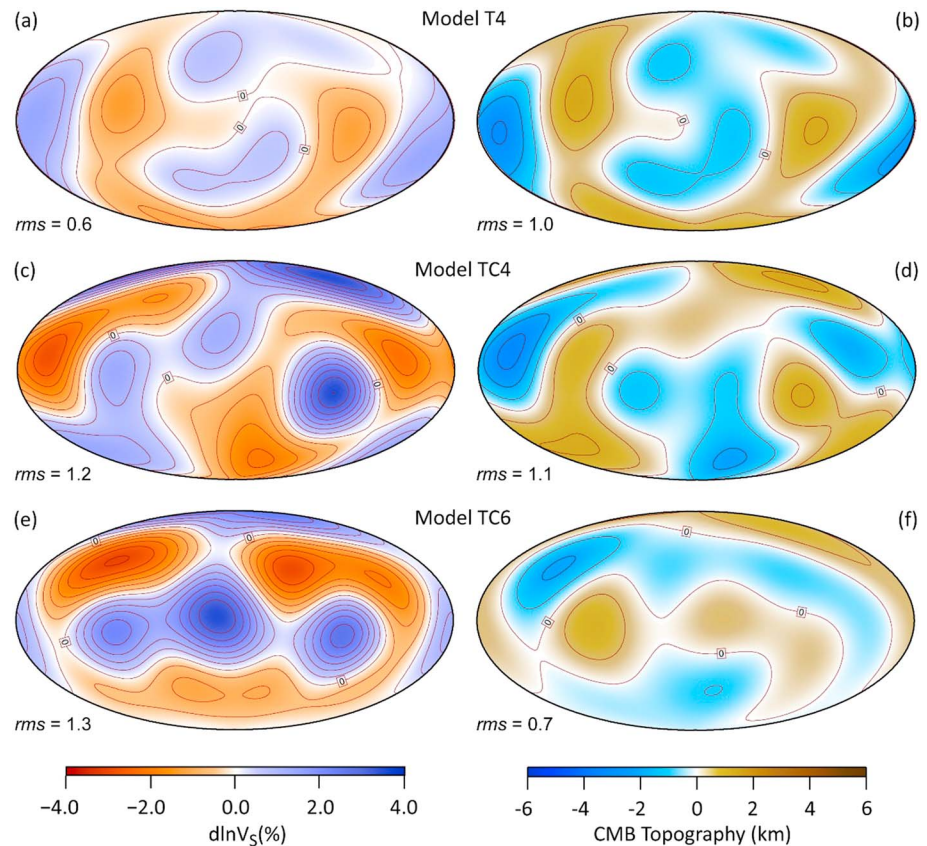
Figure 9. Shear-wave velocity anomalies in the (left column) lowermost mantle (2,700–2,891 km) and (right column) CMB dynamic topography predicted by (top row) purely thermal model T4 and thermochemical models (middle row) TC4 ($B_z = 0.23$,), and (bottom row) TC6 ($B_z = 0.15$). The viscosity ratio between postperovskite and bridgmanite is $\Delta\eta_{pPv} = 10^{-3}$ in all plots. All maps are filtered for spherical harmonic degrees up to $l = 4$. For details on the calculation of shear-wave velocity anomalies, see main text and supporting information. Intervals of contour levels are 0.5% for $dlnV_S$ and 1 km for CMB topography. Root mean square (*rms*) of each distribution is indicated at the bottom left of each plot.

($B_z = 0.15$), the correlation between long-wavelength topography and shear-wave tomography depends on $\Delta\eta_{pPv}$, these distributions being anticorrelated ($\chi = -0.50$) for regular pPv, and correlated ($\chi = 0.72$) for $\Delta\eta_{pPv} = 10^{-3}$.

It is further interesting to compare the maps of $dlnV_S$ predicted by different models with observed tomographic maps of shear-wave velocity. In particular, the $dlnV_S$ calculated by thermochemical simulations are larger than those obtained from purely thermal models by about a factor of 2 in amplitude, with *rms* relative anomalies around 0.6–0.9% for purely thermal simulations, and 1.2–1.6% for thermochemical cases. For comparison, *rms* anomaly in the lowermost layer of SB10L18 (Masters et al., 2000) is around 0.9% (Figure 10), that is, in between the anomalies reconstructed from purely thermal and thermochemical models. Note that if the contribution from postperovskite is neglected, the amplitude of $dlnV_S$ predicted by thermochemical simulations match that of SB10L18 better (Deschamps et al., 2018). It should also be kept in mind that, due to regularization, global tomography models tend to underestimate the amplitude of velocity anomalies. In addition to differences in *rms* anomalies, the patterns (Figures 8, 9, and S8) and power spectra (Figure 10) of $dlnV_S$ obtained for purely thermal and thermochemical cases strongly differ and are further affected by the value of $\Delta\eta_{pPv}$. Anomalies obtained from the thermochemical case with $\Delta\eta_{pPv} = 1$ (TC1) are dominated by spherical harmonic degree 2, in good agreement with SB10L18. As the value of $\Delta\eta_{pPv}$ drops to 10^{-3} (case TC4), degrees 3 and 4 become dominant, and the relative contributions of higher degrees are stronger. Weak thermochemical models (TC5 and TC6) are dominated by degrees 3 and 4 independently of the value of $\Delta\eta_{pPv}$. Finally, purely thermal cases are dominated by degree 2, but have flatter spectra
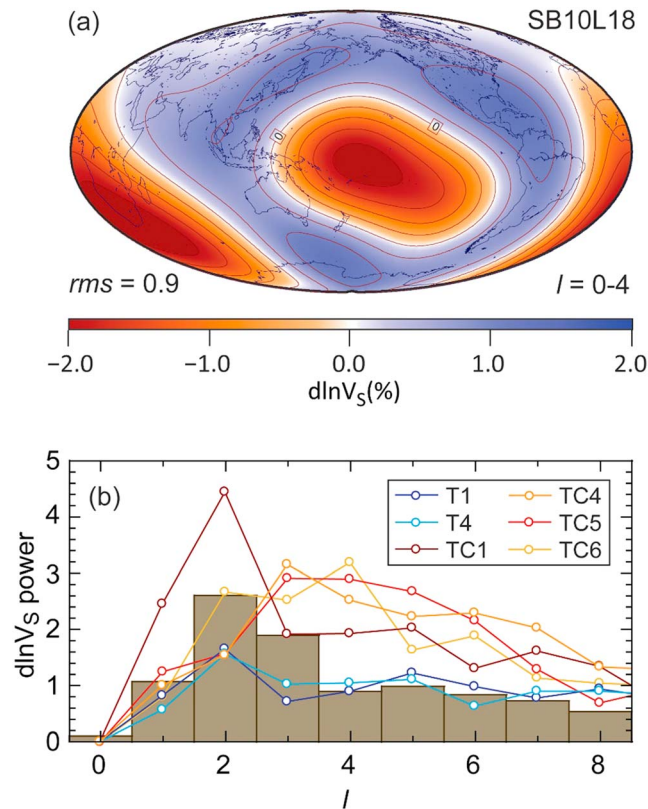
Figure 10. Long-wavelength shear-wave velocity anomalies in the lowermost mantle. (a) Lowermost layer of tomographic model SB10L18 (Masters et al., 2000) filtered for spherical harmonic degrees up to $l = 4$. Interval of contour levels is 0.5%. (b) Power spectra of SB10L18 (histogram) and of shear-velocity anomalies predicted by models T1, T4, TC1, TC4, TC5, and TC6 (curves) up to spherical harmonic degree $l = 8$.

than case TC1 for all values of $\Delta\eta_{\mathrm{pPv}}$, that is, relatively to the contribution of degree 2, the contributions of degrees $l \geq 3$ are stronger than in model TC1.

5. Concluding Discussion

In this study, we performed numerical simulations of thermal and thermochemical convection in 3-D spherical geometry to assess the influence of the viscosity of the postperovskite (pPv) phase on the dynamics of the deep mantle and on the dynamic topography at CMB. A first result is that a decrease in viscosity ratio between pPv and bridgmanite, $\Delta\eta_{\mathrm{pPv}}$, substantially influences the predicted thermochemical structure. For the values of the rheological parameters (thermal and chemical viscosity ratios) used in our simulations, weak pPv ($\Delta\eta_{\mathrm{pPv}} = 10^{-3}$) results in more stable thermochemical structures than regular pPv ($\Delta\eta_{\mathrm{pPv}} = 1$) models, and are dominated by smaller-scale (spherical harmonic degrees 3 to 6) wavelengths. Such structures are unlikely to describe the Earth's mantle, because the shear-wave velocity structures they imply do not compare well with observed seismic structure (Figures 9 and 10). Explaining the observed lowermost mantle structure would then require that the viscosities of pPv and bridgmanite are close to each other, typically within an order of magnitude. These conclusions may however change if other values of the rheological parameters are selected (see below). CMB topography is also impacted by the decrease in pPv viscosity. In particular, because the depressions caused by downwellings become shallower as pPv viscosity decreases, the peak-to-peak amplitude of topography strongly decreases, typically by a factor of 2. As a result, the amplitudes of CMB topography predicted by numerical simulations fit within observational constraints whatever the value of the pPv viscosity we considered. When filtered to long wavelengths ($l = 0–4$), predicted CMB topography and shear-wave velocity anomalies correlate in the case of strong ($\Delta\rho_{\mathrm{C}} = 140$ kg/m^3) thermochemical models, and anticorrelate in the case of purely thermal models, both trends being amplified with decreasing pPv viscosity. Interestingly, in weak thermochemical cases ($\Delta\rho_{\mathrm{C}} = 90$ kg/m^3),

long-wavelength topography and tomography are anticorrelated in the regular pPv model (case TC5; Lassak et al., 2010), but correlated in the weak pPv model (TC6).

Another interesting result of numerical simulations is that pPv viscosity strongly influences time variations in CMB (basal) heat flux, the amplitude and frequency of these variations increasing with decreasing pPv viscosity. Li et al. (2014b) reported a similar behavior for numerical experiments with $\Delta\eta_C = 1$, suggesting that this effect does not depend on other rheological parameters. A possible explanation for the large CMB heat flux variations observed in weak pPv cases is that cold downwellings being less viscous, they spread more easily around the CMB, thus inducing faster and stronger changes in local temperatures. The viscosity of pPv may further affect the spatial variations in CMB heat flux. Because *rms* in temperature anomalies above CMB increases with decreasing pPv viscosity (section 3.1 and Table 1), lateral variations in heat flux should also increase in amplitude. Amplitude of CMB heat flux variations may, in turn, have implications on core dynamics and geodynamo. Large temporal variations may explain the strong time dependence of polarity reversal of the Earth's magnetic dipole (Glatzmaier et al., 1999), including the existence of both hyperreversive periods and long periods of stability (superchrons). On another hand, large amplitude in spatial heat flux variations may lead to higher reversal frequencies (Olson & Amit, 2014).

The amount and distribution of pPv in the lowermost mantle may influence the thermochemical structures and alter our conclusions. These parameters are controlled by the assumed values of the CMB temperature, T_{CMB}, and of the properties of the bridgmanite to pPv phase transition, in particular its Clapeyron slope Γ_{pPv}. The simulations performed in this study were obtained for $T_{CMB} = 3{,}750$ K, slightly higher than the median value of current estimates of T_{CMB} (Tackley, 2012). For lower values, pPv would be stable over a wider region, and low-viscosity pPv should lead to stronger changes in topography. In particular, regions with temperatures intermediate between those of piles (or plume clusters) and downwellings should have smaller topography, and the peak-to-peak amplitude should be further reduced compared to the results obtained in this study. If, as suggested by Li et al. (2016), small patches of pPv are stable within reservoirs of dense material, the depressions caused by these reservoirs may be less flat than in our simulations, as the depth of these depressions may be locally reduced beneath pPv patches. For very low values of T_{CMB}, around 3,000–3,200 K, pPv may cover all or most of the CMB, leading to small amplitudes in CMB topography, as noted by Yoshida (2008). Similar effects are expected if reducing Γ_{pPv}, which, following Tateno et al. (2009), is fixed to 13 MPa/K in our simulations. Note that, while the values of Γ_{pPv} and T_{CMB} are still uncertain, the numerical simulations of Li et al. (2015) indicate that the values prescribed in our simulations provide a better description of lower mantle structure (as observed by seismic tomography) than other sets of these parameters.

The conclusion that the stability of thermochemical piles increases with decreasing pPv viscosity may be altered by the values of other rheological parameters, mainly the thermal and chemical viscosity ratios, $\Delta\eta_T$ and $\Delta\eta_C$. Assuming that primordial and regular mantle material have similar intrinsic viscosities ($\Delta\eta_C = 1$), Li et al. (2014b) arrived to the opposite result; that is, piles are less stable for weak pPv than for regular pPv. By contrast, increasing $\Delta\eta_T$ favors piles stability by reducing the effective viscosity of piles, which decreases, in turn, the entrainment of primordial material by plumes. The combined effect of rheological parameters on the thermochemical structure and dynamic topography is thus complex and should be studied in details, which is beyond the scope of this study. A possible scenario may however be underlined. With decreasing pPv viscosity, downwellings become less viscous and have higher velocities and kinetic energy as they reach the CMB, spread around it, and interact with piles of dense material. An increase in velocity is supported by the observation that downwellings spread more easily and rapidly around the CMB in weak pPv simulations (Li et al., 2014b). Because more kinetic energy is involved, piles are more affected by interactions with downwellings and are overall less stable. Interactions between downwellings and piles are however sensitive to the viscosity contrast between these two structures. If piles are too viscous compared to downwellings, for instance because dense material is chemically more viscous ($\Delta\eta_C > 1$), material reaching the CMB may simply glide around piles and have limited impact on these structures. In that case, low-viscosity pPv, while it allows downwellings to have higher velocity, would strongly increase the viscosity contrast between piles and surrounding material, inhibiting interaction with piles and favoring the stability of these structures. Following this reasoning, a strong thermochemical model (for instance, $B_z = 0.23$) with $\Delta\eta_C = 1$ and $\Delta\eta_{pPv} = 10^{-3}$ should lead to less stable thermochemical piles, possibly similar

to the structure obtained for a lower buoyancy ratio and $\Delta\eta_{pPv} = 1$. This may impact CMB topography, first because reducing $\Delta\eta_C$ directly induces a decrease in the amplitude of CMB topography beneath piles, which, for $\Delta\eta_{pPv} = 1$, results in a decorrelation between long-wavelength CMB topography and shear-wave velocity anomalies (Deschamps et al., 2018), and second because dynamic topography beneath piles with low density contrast is substantially reduced and is anticorrelated with shear-wave velocity anomalies at long wavelengths (Deschamps et al., 2018; Lassak et al., 2010). For weak thermochemical cases (e.g., $B_z = 0.15$), additional complexities arise, as the correlation between long-wavelength topography and shear-wave velocity tomography depends on $\Delta\eta_{pPv}$ even for $\Delta\eta_C > 1$. If this scenario is correct, and if the pPv viscosity is very low compared to that of bridgmanite, the inference of the mantle thermochemical structure based on the comparison between the large-scale CMB topography and shear-wave velocity maps would be more uncertain. However, thermochemical piles would still be expected to induce depressions in the CMB topography, in contrast to plume clusters that induce positive topography, thus providing a possible observational test based on local topography. More specifically, CMB topography in LLSVP areas, if not to small, could be locally measured using, for instance, multiple reflected wave techniques. A depression of 1–2 km in these regions would strongly support a thermochemical nature of LLSVPs.

References

Akbarashrafi, F., Al-Attar, D., Deuss, A., Trampert, J., & Valentine, A. P. (2018). Exact free-oscillation spectra, splitting functions and the resolvability of Earth's density structure. *Geophysical Journal International*, *213*(1), 58–76. https://doi.org/10.1093/gji/ggx539

Al-Attar, D., Woodhouse, J. H., & Deuss, A. (2012). Calculation of normal mode spectra in laterally heterogeneous Earth models using an iterative direct solution method. *Geophysical Journal International*, *189*(2), 1038–1046. https://doi.org/10.1111/j.1365-246X.2012.05406.x

Amman, M. W., Brodholt, J. P., Wookey, J., & Dobson, D. P. (2010). First principles constraints on diffusion in lower-mantle minerals and a weak D'' layer. *Nature*, *465*(7297), 462–465. https://doi.org/10.1038/nature09052

Bower, D. J., Gurnis, M., & Seton, M. (2013). Lower mantle structure from paleogeographically constrained dynamic Earth model. *Geochemistry, Geophysics, Geosystems*, *14*, 44–63. https://doi.org/10.1029/2012GC004267

Cobden, L. J., Thomas, C., & Trampert, J. (2015). Seismic detection of post-perovskite inside the Earth. In A. Khan, & F. Deschamps (Eds.), *The Earth's heterogeneous mantle*, (pp. 391–440). Springer. https://doi.org/10.1007/978-3-319-15627-9_13

Colombi, A., Nissen-Meyer, T., Boschi, L., & Giardini, D. (2014). Seismic waveform inversion for core-mantle boundary topography. *Geophysical Journal International*, *198*(1), 55–71. https://doi.org/10.1093/gji/ggu112

Davies, D. R., Goes, S., Davies, J. H., Schuberth, B. S. A., Bunge, H.-P., & Ritsema, J. (2012). Reconciling dynamic and seismic models of Earth's lower mantle: The dominant role of thermal heterogeneity. *Earth and Planetary Science Letters*, *353-354*, 253–269.

Davies, J. H. (2013). Global map of solid Earth heat flow. *Geochemistry, Geophysics, Geosystems*, *14*, 4608–4622. https://doi.org/10.1029/ggge.20271

Deschamps, F., Cobden, L., & Tackley, P. J. (2012). The primitive nature of large low shear-wave velocity provinces. *Earth and Planetary Science Letters*, *349-350*, 198–208.

Deschamps, F., Konishi, K., Fuji, N., & Cobden, L. (2019). Radial thermo-chemical structure beneath western and northern Pacific from seismic waveform inversion. *Earth and Planetary Science Letters*, *520*, 153–163. https://doi.org/10.1016/j.epsl.2019.05.040

Deschamps, F., Rogister, Y., & Tackley, P. J. (2018). Constraints on core-mantle boundary topography from models of thermal and thermochemical convection. *Geophysical Journal International*, *212*(1), 164–188. https://doi.org/10.1093/gji/ggx402

Deschamps, F., & Tackley, P. J. (2008). Searching for models of thermo-chemical convection that explain probabilistic tomography: I—Principles and influence of rheological parameters. *Physics of the Earth and Planetary Interiors*, *171*(1-4), 357–373. https://doi.org/10.1016/j.pepi.2008.04.016

Deschamps, F., & Tackley, P. J. (2009). Searching for models of thermo-chemical convection that explain probabilistic tomography: II—Influence of physical and compositional parameters. *Physics of the Earth and Planetary Interiors*, *176*(1-2), 1–18. https://doi.org/10.1016/j.pepi.2009.03.012

Ding, H., & Chao, B. F. (2018). A 6-year westward rotary motion in the Earth: Detection and possible MICG coupling mechanism. *Earth and Planetary Science Letters*, *495*, 50–55.

Doornbos, D. J., & Hilton, T. (1989). Models of the core-mantle boundary and the travel times of internally reflected core phase. *Journal of Geophysical Research*, *94*(B11), 15,741–15,751. https://doi.org/10.1029/JB094iB11p15741

Forte, A. M., & Peltier, R. (1991). Viscous flow models of global geophysical observables: 1. Forward problems. *Journal of Geophysical Research*, *96*(B12), 20,131–20,159. https://doi.org/10.1029/91JB01709

Garcia, R., & Souriau, A. (2000). Amplitude of the core-mantle boundary topography estimated by stochastic analysis of core phases. *Physics of the Earth and Planetary Interiors*, *117*(1-4), 345–359. https://doi.org/10.1016/S0031-9201(99)00106-5

Glatzmaier, G. A., Coe, R. S., Hongre, L., & Roberts, P. H. (1999). The role of the Earth's mantle in controlling the frequency of geomagnetic reversals. *Nature*, *401*(6756), 885–890. https://doi.org/10.1038/44776

Hernlund, J., Thomas, C., & Tackley, P. J. (2005). A doubling of the post-perovskite phase boundary and structure of the Earth's lowermost mantle. *Nature*, *434*(7035), 882–886. https://doi.org/10.1038/nature03472

Heyn, E., Conrad, C. P., & Trønnes, R. G. (2018). Stabilizing effect of compositional viscosity contrasts on thermochemical piles. *Geophysical Research Letters*, *45*, 7523–7532. https://doi.org/10.1029/2018GL078799

Ishii, M., & Tromp, J. (1999). Normal-mode and free-air gravity constraints on lateral variations in velocity and density of Earth's mantle. *Science*, *285*(5431), 1231–1236. https://doi.org/10.1126/science.285.5431.1231

Jaupart, C., Labrosse, S., Lucazeau, F., & Mareschal, J.-C. (2015). Temperature, heat, and energy in the mantle of the Earth. In G. Schubert (Ed.), *Treatise on Geophysics*, (2nd ed., Vol. 7, pp. 218–251). Elsevier.

Kellogg, L. H., Hager, B. H., & van der Hilst, R. D. (1999). Compositional stratification in the deep mantle. *Science*, *283*(5409), 1881–1884. https://doi.org/10.1126/science.283.5409.1881

Koelemeijer, P., Deuss, A., & Ritsema, J. (2017). Density structure of Earth's lowermost mantle from Stoneley mode splitting observations. *Nature Communications*, *8*(1). https://doi.org/10.1038/ncomms15241

Koelemeijer, P. J., Deuss, A., & Trampert, J. (2012). Normal mode sensitivity to Earth's *D″* layer and topography on the core-mantle boundary: What we can and cannot see. *Geophysical Journal International*, *190*(1), 553–568. https://doi.org/10.1111/j.1365-246X.2012.05499.x

Koper, K. D., Pyle, M. L., & Franks, J. M. (2003). Constraints on aspherical core structure from PKiKP-PcP differential travel times. *Journal of Geophysical Research*, *108*(B3), 2618. https://doi.org/10.1029/2002JB001995

Lassak, T. M., McNamara, A. K., Garnero, E. J., & Zhong, S. (2010). Core–mantle boundary topography as a possible constraint on lower mantle chemistry and dynamics. *Earth and Planetary Science Letters*, *289*, 232–241.

Lau, H. C. P., Mitrovica, J. X., Davis, J. L., Tromp, J., Yang, H.-Y., & Al-Attar, D. (2017). Tidal tomography constraints Earth's deep mantle buoyancy. *Nature*, *551*(7680), 321–326. https://doi.org/10.1038/nature24452

Li, Y., Deschamps, F., & Tackley, P. J. (2014a). The stability and structure of primordial reservoirs in the lower mantle: Insights from models of thermo-chemical convection in 3-D spherical geometry. *Geophysical Journal International*, *199*(2), 914–930. https://doi.org/10.1093/gji/ggu295

Li, Y., Deschamps, F., & Tackley, P. J. (2014b). Effects of low-viscosity post-perovskite on the stability and structure of primordial reservoirs in the lower mantle. *Geophysical Research Letters*, *41*, 7089–7097. https://doi.org/10.1002/2014GL061362

Li, Y., Deschamps, F., & Tackley, P. J. (2015). Effects of the post-perovskite phase transition properties on the stability and structure of primordial reservoirs in the lower mantle of the Earth. *Earth and Planetary Science Letters*, *432*, 1–12.

Li, Y., Deschamps, F., Tackley, P. J., & P. J. (2016). Small post-perovskite patches at the base of lower mantle primordial reservoirs: Insights from 2-D numerical modeling and implications for ULVZs. *Geophysical Research Letters*, *43*, 3215–3225. https://doi.org/10.1002/2016GL067803

Masters, G., Laske, G., Bolton, H., & Dziewonski, A. M. (2000). The relative behavior of shear velocity, bulk sound speed, and compressional velocity in the mantle: Implication for thermal and chemical structure. In S.-I. Karato, et al. (Eds.), *Earth's deep interior: Mineral physics and tomography from the atomic to the global scale*, *Geophysical Monograph Ser.*, (Vol. 117, pp. 63–87). Washington DC: American Geophysical Union.

McNamara, A. K., & Zhong, S. (2004). Thermochemical structures within a spherical mantle. *Journal of Geophysical Research*, *109*, B07402. https://doi.org/10.1029/2003JB002847

Morelli, A., & Dziewonski, A. M. (1987). Topography of the core-mantle boundary and lateral homogeneity of the liquid core. *Nature*, *325*(6106), 678–683. https://doi.org/10.1038/325678a0

Mosca, I., Cobden, L., Deuss, A., Ritsema, J., & Trampert, J. (2012). Seismic and mineralogical structures of the lower mantle from probabilistic tomography. *Journal of Geophysical Research*, *117*, B06304. https://doi.org/10.1029/2011JB008851

Moulik, P., & Ekström, G. (2016). The relationships between large-scale variations in shear velocity, density, and compressional velocity in the Earth's mantle. *Journal of Geophysical Research: Solid Earth*, *121*, 2737–2771. https://doi.org/10.1002/2015JB012679

Mulyukova, E., Steinberger, B., Dabrowski, M., & Sobolev, S. V. (2015). Survival of LLSVPs for billions of years in a vigorously convecting mantle: Replenishment and destruction of chemical anomaly. *Journal of Geophysical Research: Solid Earth*, *120*, 3824–3847. https://doi.org/10.1002/2014JB011688

Murakami, M., Hirose, K., Kawamura, K., Sata, N., & Ohishi, Y. (2004). Post-perovskite phase transition in MgSiO₃. *Science*, *304*(5672), 855–858. https://doi.org/10.1126/science.1095932

Nakagawa, T., & Tackley, P. J. (2005). The interaction between the post-perovskite phase change and a thermo-chemical boundary layer near the core-mantle boundary. *Earth and Planetary Science Letters*, *238*, 204–216.

Oganov, A. R., & Ono, S. (2004). Theoretical and experimental evidence for a post-perovskite phase of MgSiO₃ in Earth's *D″* layer. *Nature*, *430*(6998), 445–448. https://doi.org/10.1038/nature02701

Olson, P., & Amit, H. (2014). Magnetic reversal frequency scaling in dynamos with thermochemical convection. *Physics of the Earth and Planetary Interiors*, *229*, 122–133. https://doi.org/10.1016/j.pepi.2014.01.009

Richter, F. M. (1985). Models for the Archean thermal regime. *Earth and Planetary Science Letters*, *73*, 350–360.

Soldati, G., Koelemeijer, P., Boschi, L., & Deuss, A. (2013). Constraints on core-mantle boundary topography from normal mode splitting. *Geochemistry, Geophysics, Geosystems*, *14*, 1333–1342. https://doi.org/10.1002/ggge.20115

Sze, E. K. M., & van der Hilst, R. D. (2003). Core mantle boundary topography from short period PcP, PKP, and PKKP data. *Physics of the Earth and Planetary Interiors*, *135*(1), 27–46. https://doi.org/10.1016/S0031-9201(02)00204-2

Tackley, P. J. (2012). Dynamics and evolution of the deep mantle resulting from thermal, chemical, phase and melting effects. *EarthSci. Rev.*, *110*, 1–25.

Tackley, P. J. (2008). Modelling compressible mantle convection with large viscosity contrasts in a three-dimensional spherical shell using the yin-yang grid. *Physics of the Earth and Planetary Interiors*, *171*(1-4), 7–18. https://doi.org/10.1016/j.pepi.2008.08.005

Tanaka, S. (2010). Constraints on the core-mantle boundary topography from P4KP-PcP differential travel times. *Journal of Geophysical Research*, *115*, B04310. https://doi.org/10.1029/2009JB006563

Tateno, S., Hirose, K., Sata, N., & Ohishi, Y. (2009). Determination of post-perovskite phase transition boundary up to 4400 K and implications for thermal structure in *D″* layer. *Earth and Planetary Science Letters*, *277*, 130–136.

Trampert, J., Deschamps, F., Resovsky, J. S., & Yuen, D. A. (2004). Probabilistic tomography maps significant chemical heterogeneities in the lower mantle. *Science*, *306*(5697), 853–856. https://doi.org/10.1126/science.1101996

Yamazaki, D., & Karato, S.-I. (2001). Some mineral physics constraints on the rheology and geothermal structure of Earth's lower mantle. *American Mineralogist*, *86*(4), 385–391. https://doi.org/10.2138/am-2001-0401

Yang, H.-Y., & Tromp, J. (2015). Synthetic free-oscillation spectra: An appraisal of various mode-coupling methods. *Geophysical Journal International*, *203*(2), 1179–1192. https://doi.org/10.1093/gji/ggv349

Yoshida, M. (2008). Core-mantle boundary topography estimated from numerical simulations of instantaneous mantle flow. *Geochemistry, Geophysics, Geosystems*, *9*, Q07002. https://doi.org/10.1029/2008GC002008

Zhang, S., & Christensen, U. (1993). Some effects of lateral viscosity variations on geoid and surface velocities induced by density anomalies in the mantle. *Geophysical Journal International*, *114*(3), 531–547. https://doi.org/10.1111/j.1365-246X.1993.tb06985.x